MJO Propagation Shaped by Zonal Asymmetric Structures: Results from 24 GCM Simulations

BIN WANG

Department of Atmospheric Sciences and International Pacific Research Center, University of Hawai'i at Mānoa, Honolulu, Hawaii, and Earth System Modeling Center, Nanjing University of Information Science and Technology, Nanjing, China

SUN-SEON LEE

Department of Atmospheric Sciences and International Pacific Research Center, University of Hawai'i at Mānoa, Honolulu, Hawaii

(Manuscript received 4 December 2016, in final form 30 June 2017)

ABSTRACT

Eastward propagation is an essential characteristic of the Madden–Julian oscillation (MJO). Yet, simulation of MJO propagation in general circulation models (GCMs) remains a major challenge and understanding the causes of propagation remains controversial. The present study explores why the GCMs have diverse performances in MJO simulation by diagnosis of 24 GCM simulations. An intrinsic linkage is found between MJO propagation and the zonal structural asymmetry with respect to the MJO convective center. The observed and realistically simulated MJO eastward propagations are characterized by stronger Kelvin easterly waves than Rossby westerly waves in the lower troposphere, which is opposite to the Gill pattern where Rossby westerly waves are 2 times stronger than Kelvin easterly waves. The GCMs simulating stronger Rossby westerly waves tend to show a stationary MJO. MJO propagation performances are robustly correlated with the quality of simulated zonal asymmetries in the 850-hPa equatorial zonal winds, 700-hPa diabatic heating, 1000–700-hPa equivalent potential temperature, and convective instability. The models simulating realistic MJO propagation are exemplified by an eastward propagation of boundary layer moisture convergence (BLMC) that leads precipitation propagation by about 5 days. The BLMC stimulates MJO eastward propagation by preconditioning and predestabilizing the atmosphere, and by generating lower-tropospheric heating and available potential energy to the east of precipitation center. The MJO structural asymmetry is generated by the three-way interaction among convective heating, moisture, and equatorial wave and boundary layer dynamics. In GCMs, differing convective heating representation could produce different MJO structural asymmetry, and thus different propagations. Diagnosis of structural asymmetry may help revealing the models' deficiency in representing the complex three-way interaction processes, which involves various parameterized processes.

1. Introduction

Aiming at reducing deficiencies in the simulation of the Madden–Julian oscillation (MJO) in general circulation models (GCMs), the World Climate Research Programme (WCRP)–World Weather Research Programme (WWRP)/THORPEX MJO Task Force and Year of Tropical Convection (YOTC) and the GEWEX Atmosphere System Study (GASS) launched a suite of modeling experiments (Klingaman et al. 2015a). There was a 20-yr simulation component aiming at characterization of models' capability in representing intrinsic MJO variability and exploration of key processes responsible for high-quality representation of the MJO (Jiang et al. 2015, hereafter J15). This dataset provides an excellent opportunity for understanding the mechanisms driving MJO eastward movement, which remains under debate so far.

Models in which convective parameterization schemes are more sensitive to the effects of free-tropospheric humidity tend to produce a more robust MJO (e.g., Hannah and Maloney 2011). This knowledge has led to the development of moisture mode theory in

School of Ocean and Earth Science and Technology Publication Number 10073, International Pacific Research Center Publication Number 1275, and Earth System Modeling Center Publication Number 165.

Corresponding author: Bin Wang, wangbin@hawaii.edu

DOI: 10.1175/JCLI-D-16-0873.1

which processes associated with tropospheric moisture are considered as key elements shaping the MJO dynamics (Raymond and Fuchs 2009; Sobel and Maloney 2012, 2013; Adames and Kim 2016). Recent studies of processes-oriented diagnostics have primarily focused on the role of convection–moisture interaction and the importance of the sensitivity of parameterized convection to environmental moisture for GCM representations of the MJO (Thayer-Calder and Randall 2009; Kim et al. 2012; Xavier 2012). Observed precipitation rate is a strong nonlinear function of saturation fraction or vertical relative humidity (RH) profile (Bretherton et al. 2004). With 27 model simulations from the process-oriented MJO diagnostic project, J15 confirmed the results of Kim et al. (2014b) and showed that the difference in the 850–500-hPa RH between top 5% and bottom 10% of precipitation events is significantly correlated with the MJO propagation fidelity, but the correlation coefficient (CC) is only 0.45. Klingaman et al. (2015b), based on their analysis of the 13 models' 20-day hindcast experiments, found no link between the hindcast fidelity and the precipitation–moisture relationship. Another diagnostic of the processes that control tropospheric moisture is gross moist stability (GMS), which represents the efficiency with which convection discharges moisture from the atmospheric column (Raymond et al. 2009). J15 explored how seasonal mean GMS is related to MJO propagation fidelity and found a marginally significant negative correlation (CC = −0.36) between the simulated winter mean vertical GMS and the MJO propagation fidelity over the Indo-Pacific Ocean. This is consistent with the results of Raymond et al. (2009) and Benedict et al. (2014). On the other hand, J15 found a robust correlation between MJO propagation and the pattern correlation coefficient (PCC) of the vertical structures of vertical velocity (CC = 0.78) and diabatic heating (CC = 0.70). But the reasons remain elusive. We argue that the westward tilts with height of upward motion and heating occur primarily in the lower troposphere, and hence it is important to understand the roles of the lower-tropospheric processes in MJO propagation and the important role of the interactions among the diabatic heating, moistening, and the large-scale circulation (especially the wave and boundary layer dynamics). This is our major starting point.

Our analysis is also motivated by previously observed relationships between MJO low-level structure and eastward propagation. The MJO has a gross baroclinic vertical structure with a low (sea level) pressure and boundary layer moisture convergence (BLMC) leading the major convective center (Madden and Julian 1972; Wang 1988; Hendon and Salby 1994; Salby et al. 1994; Jones and Weare 1996; Matthews 2000; Sperber 2003; Lin et al. 2004; Tian et al. 2006; J15). Observations also firmly established that to the east of the MJO convective center occur gradual deepening of the moist boundary layer (Johnson et al. 1999; Kemball-Cook and Weare 2001; Tian et al. 2006), gradual increase of convective instability (Hsu and Li 2012), and a transition from cumulus congestus clouds to deep convection (Kikuchi and Takayabu 2004; Katsumata et al. 2009; Virts and Wallace 2010; Del Genio et al. 2012; Johnson et al. 2015). These structural features have been suggested in favor of MJO eastward propagation. We are curious about whether the GCMs that capture these structural features better simulate MJO propagation.

Another motivation for this work comes from a recent finding in a theoretical study. In a general theoretical model for MJO with different cumulus parameterizations, the eastward propagation speeds of the MJO modes are found to be inversely related to the relative strengths of the equatorial Rossby westerly wave and the Kelvin easterly wave (Wang and Chen 2017). It would be interesting to see how GCM-simulated MJO propagation is related to the MJO low-level structural asymmetry.

In the present study, we use 24 sets of GCM simulation data collected by the "Vertical Structure and Diabatic Processes of the MJO: A Global Model Evaluation Project" (Petch et al. 2011) to examine the relationship between MJO propagation and its lower-tropospheric dynamic and thermodynamic structures and the BLMC-related processes. Section 2 depicts the data and method used. Section 3 discusses briefly how to measure the models' performance for simulating MJO propagation. Section 4 contrasts the characteristics of the simulated MJO in two groups of models (eastward-propagating and nonpropagating MJO models), which reveal salient differences in their structures. Section 5 further documents the intrinsic linkages between MJO propagation and its zonal asymmetric structure using all model simulations. In section 6, we discuss how the MJO structural asymmetry leads to eastward propagation. The last section provides a summary and discusses the root cause of the MJO structural asymmetry and implications of the results for improvement of GCM simulations.

2. Data and method

We use GPCP daily precipitation data (Huffman and Bolvin 2013) for the period 1997–2014 (18 yr). For the horizontal and vertical wind, temperature, specific humidity, and diabatic heating, the ERA-Interim daily data with the 1.5° longitude × 1.5° latitude horizontal resolution (Dee et al. 2011) are utilized. For all results in

TABLE 1. A list of models participating in the 20-yr climate simulations. [Expansions of most model acronyms are available online at http://www.ametsoc.org/PubsAcronymList. The exceptions are listed here: BCC Atmospheric GCM version 2 (BCC-AGCM2), CAM5 with Zhang–McFarlane (ZM) convective parameterization (CAM5-ZM), CNRM Amospheric Model (CNRM-AM), CNRM ARPEGE Coupled with Météo-France Multiscale Chemistry and Transport Model (MOCAGE) (CNRM-ACM), EC-EARTH version 3 (ECEarth3), Environment Canada Global Environment Model (EC-GEM), ECHAM5 with Snow–Ice–Thermocline Coupler (ECHAM5-SIT), Iowa State University GCM (ISUGCM), Navy Global Environmental Model version 1 (NavGEM1), Pusan National University Climate Forecast System (PNU-CFS), superparameterized CAM3 (SPCAM3), superparameterized CCSM3 (SPCCSM3), and University of California San Diego CAM3 (UCSD-CAM3).]

Model name	Institution	References
ACCESS1	Centre for Australian Weather and Climate Research, Australia	Zhu et al. (2013)
BCC-AGCM2	Beijing Climate Center, China Meteorological Administration, China	Wu et al. (2010]
CAM5	National Center for Atmospheric Research, United States	Neale et al. (2012)
CAM5-ZM	Lawrence Livermore National Laboratory, United States	Song and Zhang (2011]
CanCM4	Canadian Centre for Climate Modelling and Analysis, Canada	Merryfield et al. (2013)
CFSv2	NOAA/NCEP Climate Prediction Center, United States	Saha et al. (2014)
CNRM-AM	Centre National de la Recherche Scientifique/Météo-France, France	Voldoire et al. (2013)
CNRM-CM		
CNRM-ACM		
ECEarth3	Rossby Centre, Swedish Meteorological and Hydrological Institute, Sweden	—
EC-GEM	Environment Canada, Canada	Côté et al. (1998)
ECHAM5-SIT	Academia Sinica, Taiwan	Tseng et al. (2015)
ECHAM6	Max Planck Institute for Meteorology, Germany	Stevens et al. (2013)
FGOALS-s2	Institute of Atmospheric Physics, Chinese Academy of Sciences, China	Bao et al. (2013]
GEOS-5	NASA Global Modeling and Assimilation Office, United States	Molod et al. (2012)
GISS-E2	NASA Goddard Institute for Space Studies, United States	Schmidt et al. (2014]
ISUGCM	Iowa State University, United States	Wu and Deng (2013)
MIROC5	Atmosphere and Ocean Research Institute (AORI)/National Institute for Environmental Studies (NIES)/JAMSTEC, Japan	Watanabe et al. (2010]
MRI-AGCM	Meteorological Research Institute, Japan	Yukimoto et al. (2012)
NavGEM1	U.S. Naval Research Laboratory, United States	—
PNU-CFS	Pusan National University, South Korea	Saha et al. (2006)
SPCAM3	Colorado State University, United States	Khairoutdinov et al. (2008)
SPCCSM3	George Mason University, United States	Stan et al. (2010)
UCSD-CAM3	Scripps Institution of Oceanography, United States	Zhang and Mu (2005)

the present study, intraseasonal (20–70 day) bandpass-filtered anomalies during boreal winter (from November to April) are analyzed. The data are interpolated and averaged to a 2.5° × 2.5° grid in order to match the model output.

A total of 24 sets of simulation data from 22 GCMs are analyzed (Table 1). J15 analyzed 27 model simulations, but we used data from only 24 because the results from three models, Central Weather Bureau (Taiwan) Global Forecast System (CWB-GFS), Met Office Unified Model Global Atmosphere 3 (MetUM GA3), and Texas A&M University Community Atmosphere Model, version 4 (TAMU-CAM4), were not available when we downloaded the model data. The Vertical Structure and Diabatic Processes of the MJO: A Global Model Evaluation Project (Petch et al. 2011) aims to characterize, compare, and evaluate the heating, moistening, and momentum mixing processes associated with the MJO that are produced by current global weather and climate models (http://www.cgd.ucar.edu/projects/yotc/mjo/vertical.html). Three types of simulations were carried out; we used the data from the 20-yr climate simulations, which were integrated for 20 yr and provided 6-hourly data with 2.5° × 2.5° horizontal resolutions and 22 vertical pressure levels. The detailed description of the project and models can be found in J15.

3. Measure of simulated eastward propagation of MJO

During boreal winter (from 1 November to 30 April), the organized eastward propagation of the MJO is most prominent and regular (e.g., Wang and Rui 1990; Waliser 2006; Kikuchi et al. 2012). It has been a common practice to use eastward propagation to represent the quality of the simulated MJO, but how to quantitatively and objectively measure MJO propagation skills is not a simple matter and deserves a detailed discussion. A simple way of measuring MJO propagation is to examine the longitudinal variations of the lead–lag correlation (or regression) of precipitation with reference to the MJO precipitation anomalies averaged over some reference regions (e.g., Waliser et al. 2009; J15). For

TABLE 2. Differences in definition of good and poor models between the present study and J15.

	Present study	J15
Reference points	IO: 10°S–10°N, 80°–100°E MC: 10°S–10°N, 110°–130°E WP: 10°S–10°N, 140°–160°E	IO: 5°S–5°N, 75°–85°E — WP: 5°S–5°N, 130°–150°E
Statistics	Correlation map	Regression map
Filtering and domain for PCC calculation	20–70-day filtering, 50°E–180° and from day −20 to day 20.	20–100-day filtering, 60°E–180° and from day −20 to day 20.
Definition for good and poor models	Averaged PCC skill score at the three MJO propagation diagrams derived with reference to the MJO rainfall anomalies over the IO, MC, and WP.	Averaged PCC skill score at the two MJO propagation diagrams derived with reference to the MJO rainfall anomalies over the IO and WP.

simplicity, we refer to this type of lead–lag correlation maps as an MJO propagation diagram. Here we used a procedure similar to that of J15 with some modifications as indicated in Table 2. We considered a 20–70-day filter rather than a broad filter of 20–100 days; we used precipitation in three reference locations rather than two in deriving lead–lag correlation maps for a more complete evaluation of the eastward propagation of precipitation in the eastern Hemisphere; and over the Indian Ocean (IO) we used a bigger box (10°S–10°N, 80°–100°E) as reference location rather than 5°S–5°N, 75°–85°E because we want to focus on large-scale MJO structure and movement.

Figures 1a–c show the MJO propagation diagrams with reference to the IO, Maritime Continent (MC), and western Pacific (WP) rainfall anomalies, respectively. For brevity, the model simulations are shown only for the two best and two worst models. Figure 1d compares the PCC skills (50°E–180°, from day −20 to day 20) of each model with reference to the three key reference regions. It is interesting to note that the PCC skill with reference to the IO is highly correlated with that with reference to the MC (CC = 0.96) and to a large degree with that measured at WP (CC = 0.84). The drop of correlation with the WP is mainly due to the differences in the three poorest models. In general, the skill averaged over the three reference regions may better reflect the overall propagation performance than that measured over the individual reference region. Therefore, in the present study, the model simulated MJO propagation performance is measured by the averaged PCC skill score at the three MJO propagation diagrams derived with reference to the MJO rainfall anomalies over the IO, MC, and WP (Fig. 1d). Note that the averaged skill score represents very well those skill scores with respect to the IO (CC = 0.98) and the MC (0.99), as well the WP (0.92).

Overall, higher PCC skills correspond to more systematic eastward propagation of both the wet and dry anomalies and better propagation speeds over the equatorial Indo-Pacific warm pool regions. However, the PCC skill is an overall assessment of the propagation feature; it cannot distinguish the quality in simulated propagation speed and propagation extent. There are other statistical measures of MJO propagation. Often used is the ratio of spectral power for the eastward- and westward-propagating components (the east-to-west ratio) on the MJO time and spatial scales based on the space–time power spectrum of the equatorial rainfall (Kim et al. 2009). This spectral measure has been shown to be very well correlated with the PCC skill in the propagation diagram (CC = 0.78 for 27 simulations) (J15).

4. Contrasting MJO structures in the good and poor models

The contrasting features between the good and poor models can reveal salient differences in the MJO dynamic and thermodynamic structures. Based on the averaged PCC skills of the eastward propagation of precipitation with reference to the precipitation anomalies at three key locations (Fig. 1d), we selected the top six models that simulate eastward propagation of MJO most realistically (hereafter good models) and the six poorest models that show no eastward propagation of MJO (hereafter poor models). The six best (poorest) models are CNRM-CM, SPCCSM3, ECHAM5-SIT, GISS-E2, SPCAM3, and PNU-CFS (ISUGCM, CanCM4, MIROC5, BCC-AGCM2, NavGEM1, and CFSv2) (see Table 1). All regressed MJO dynamic and thermodynamic anomalies are computed with respect to the IO precipitation anomalies because MJO precipitation and circulation over the IO are more symmetric about the equator and less affected by the basic climatological mean circulations compared to those over the MC and WP, and thus more suitable for study of the MJO structure without mean flow impacts.

a. Low-level (850 hPa) horizontal circulation

Figure 2a shows that when the MJO precipitation center is located in the equatorial IO around 90°E, the

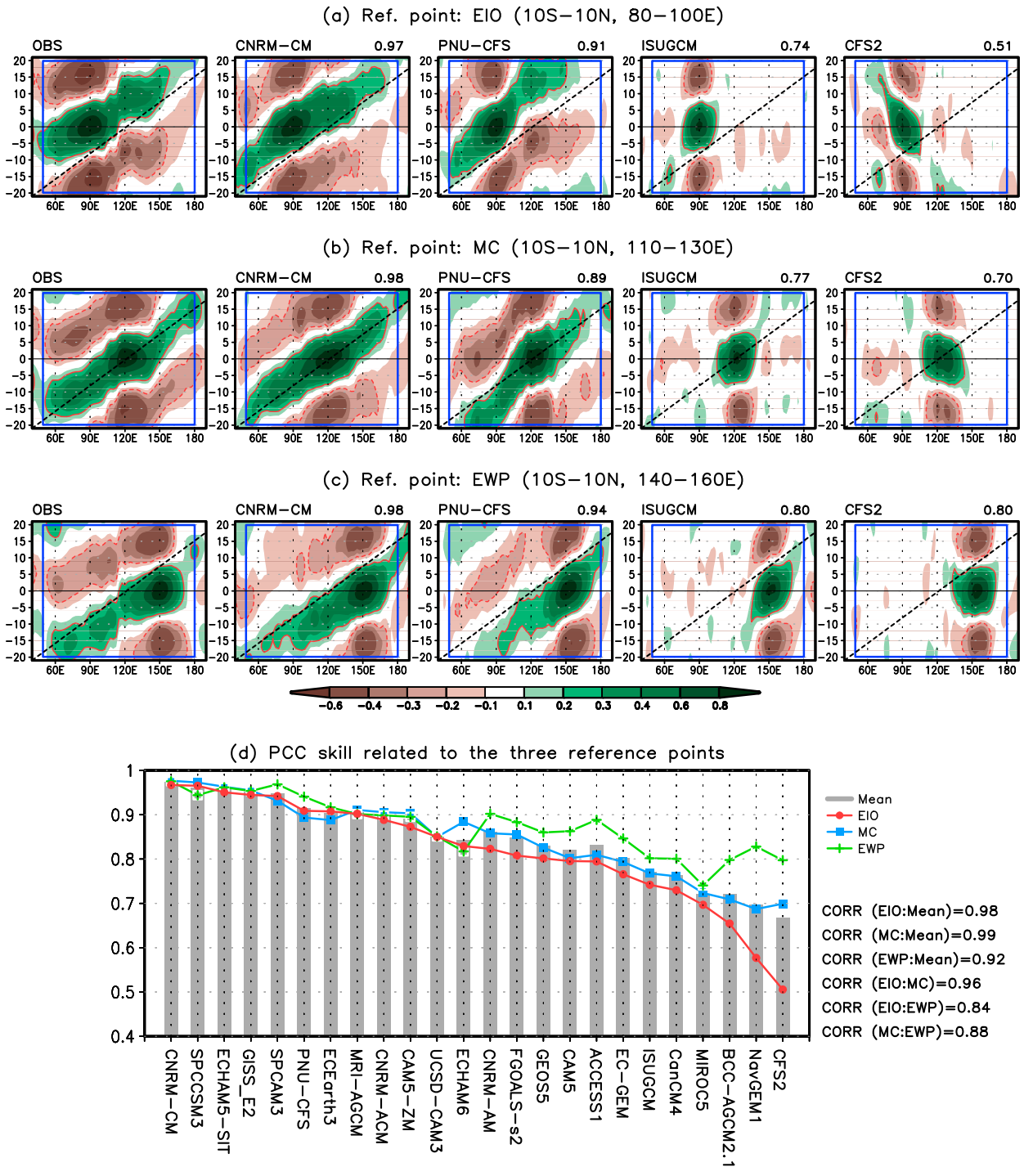

FIG. 1. Eastward propagation of MJO in observations and GCM simulations as shown by the lead–lag correlation of 20–70-day bandpass-filtered precipitation averaged over 10°S–10°N with reference to itself over the (a) equatorial Indian Ocean (EIO; 10°S–10°N, 80°–100°E), (b) Maritime Continent (10°S–10°N, 110°–130°E), and (c) equatorial western Pacific (EWP; 10°S–10°N, 140°–160°E), during boreal winter (November–April). (left)–(right) Correlation fields in observation and four GCMs are presented. (d) The PCC skill of 24 GCM simulations related to the three reference points. The gray bar indicates the mean of three PCC skills for each model. The PCC skill is calculated where correlation coefficient in observation is greater than $|\pm 0.2|$ on the time–longitude domain (50°E–180°, from day −20 to day 20; blue rectangles). The number at the top-right corner in (a)–(c) is the PCC between the observation and model simulation.

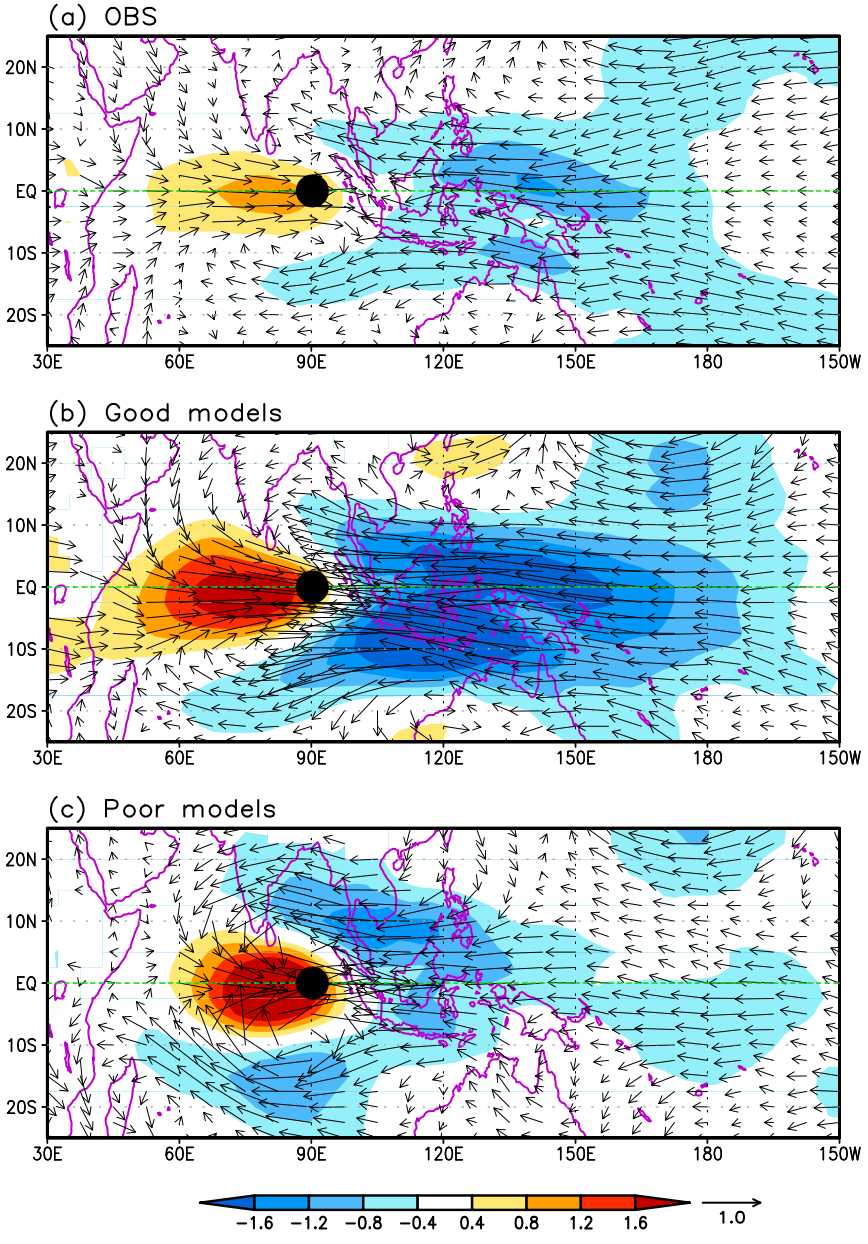

FIG. 2. Comparison of the MJO low-level horizontal structure: 850-hPa wind ($m\,s^{-1}$; vector) and U850 ($m\,s^{-1}$; shading): (a) observation, (b) composite of good model simulations, and (c) composite of poor model simulations. The structures are regressed 20–70-day bandpass-filtered fields with reference to the precipitation anomaly in the EIO (10°S–10°N, 80°–100°E). The precipitation center is marked by a black filled circle. The regression strengths are scaled to a fixed $3\,mm\,day^{-1}$ precipitation rate. See text for more details in defining the good and poor models.

observed 850-hPa winds exhibit a coupled structure of the equatorial Kelvin wave and the most trapped equatorial Rossby wave. The Rossby wave component (double cyclones and the equatorial westerly anomalies in between) is located to the west and the Kelvin wave component (the equatorial easterly and low pressure anomalies) is located to the east of the MJO precipitation center. The result here is consistent with the structure derived using other methods, such as those of Rui and Wang (1990) and Adames and Wallace (2014).

We note that the observed MJO structure shown in Fig. 2a is often referred to as a Gill pattern (Gill 1980). However, the circulation structure of the Gill pattern

differs from the MJO structure in Fig. 2a. While both consist of Rossby wave and Kelvin wave components, they have important differences in the relative strength and zonal extent of the Kelvin and Rossby wave components. In the present study, the strength and zonal extent of Kelvin and Rossby wave components are calculated using 850-hPa zonal wind (U850) averaged along the equator between 5°S and 5°N. The Kelvin–Rossby (K-R) zonal extent ratio, which is the ratio of longitudinal extent of the Kelvin easterly wave to that of the Rossby westerly wave, is 3.0 in the Gill pattern but only 2.1 in the observed MJO; the ratio of the maximum Rossby westerly wind speed versus the maximum Kelvin easterly wind speed is 2.2 in the Gill pattern but only 0.8 in the observed MJO (Fig. 2a). These notable differences arise from the nature of the precipitation heating. In the Gill model, the heating is given as a forcing and the waves are passive responses, whereas in the MJO the heating is interactive with the dynamics, thus the dynamics can feed back to the heating.

The observed low-level circulation structures are reproduced well in the good models' composite (Fig. 2b) but poorly in the poor models (Fig. 2c). The noticeable difference between the good and poor models lies in the zonal asymmetries in the intensity and zonal extent of the equatorial Kelvin easterly (wave) and Rossby westerly (wave). For poor models, the maximum Rossby westerly is notably stronger than the maximum Kelvin easterly, whereas for good models the Kelvin easterly is stronger than Rossby westerly. Note also that, for a given MJO precipitation rate of 3 mm day^{-1}, both groups of GCMs tend to produce stronger wind responses than the observations, especially the equatorial westerly anomalies. As shown later (see Fig. 10), the maximum heating center is located around 420 hPa in the observation, while it is around 460 hPa in the good models and 500 hPa in the poor models. So, the model-simulated heating profiles tend to have a lower maximum than observations. In addition, the vertical heating gradients below 600 hPa simulated in the good models are twice large as those in the observations; even in the poor models this vertical gradient is also higher than the observation. The strong responses of the low-level circulations in the models seem to be related to the lower maximum heating and larger vertical heating gradients in the lower troposphere.

b. *The 700-hPa diabatic heating and boundary layer moisture convergence*

Figure 3 displays the structures of the BLMC at 925 hPa and the diabatic heating rate at 700 hPa (Q700). Note that in observations the BLMC almost coincides with the Q700 with a PCC (15°S–15°N, 70°–150°E) reaching −0.80, indicating that the Q700 is closely associated with the 925-hPa moisture convergence. Both fields extend 5000–6000 km east of the IO precipitation center and lead the 500-hPa maximum upward motion (which almost overlaps the MJO precipitation center), implying a rearward tilt of the vertical motion with height in the lower troposphere. This has been documented by many previous studies (e.g., Hendon and Salby 1994; Sperber 2003; Tian et al. 2006; J15). The two observed characteristic features of the BLMC and Q700 fields are very well reproduced in the good models (Fig. 3b) but are absent in the poor models (Fig. 3c). The major differences between the good and poor models lie in the zonal asymmetry of the BLMC and Q700 with regard to the MJO precipitation anomaly.

c. *Lower-tropospheric equivalent potential temperature and specific humidity*

The equivalent potential temperature (EPT) is a measure of moist static energy (MSE) and its vertical gradient can indicate convective instability if the layer is bodily lifted to become saturated. Increased moisture content or temperature can make the EPT higher. Since vertical temperature gradient variation is small in the tropics, the EPT in the lower troposphere varies primarily with moisture content. Because the BLMC accumulates moisture to the east of the MJO precipitation, higher EPT is anticipated to the east of the precipitation center, with lower EPT to the west.

Figure 4 confirms the above assertion. The observed 850-hPa specific humidity and the EPT vertically averaged from 1000 to 700 hPa ($EPT_{1000–700}$) anomalies share very similar spatial patterns with a PCC (15°S–15°N, 70°–150°E) of 0.91 (Fig. 4a). Both follow the BLMC, suggesting that the BLMC controls both. The BLMC also largely determines the convective instability of the MJO (Hsu and Li 2012). The observed structures of 850-hPa specific humidity and $EPT_{1000–700}$ are faithfully reproduced by the good models (Fig. 4b), but these characteristic features are deficient in the poor models (Fig. 4c). Similar to the BLMC and Q700 structures, the major differences between the good and poor models again lie in their zonal asymmetry with regard to the MJO precipitation center.

5. Intrinsic linkages between MJO propagation and its zonal asymmetric structures

The salient differences between the good and poor models motivate us to further explore the relationships between MJO propagation and its lower-tropospheric structures using all 24 GCM simulations. For better illustration of the equatorial zonal asymmetry, all examined fields in this section were averaged along the equator

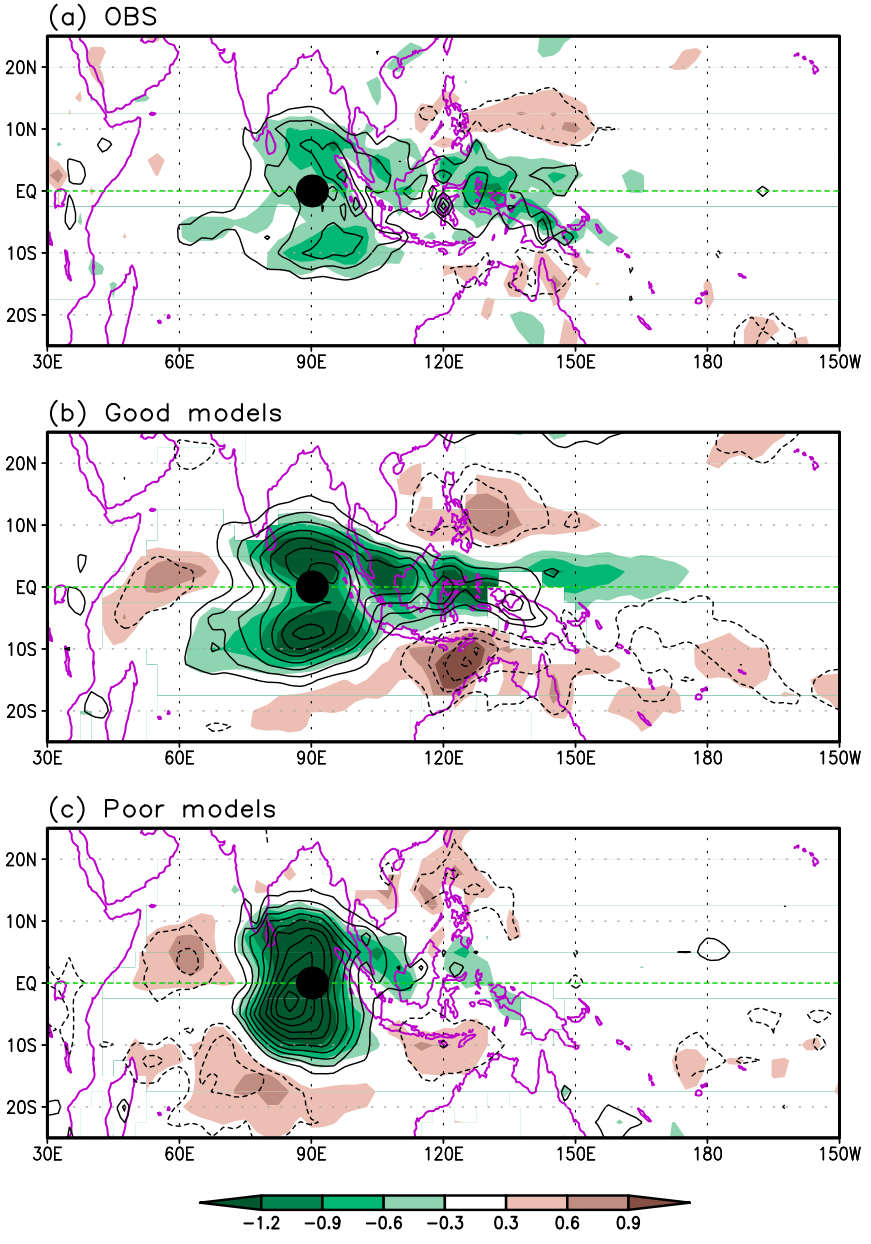

FIG. 3. As in Fig. 2, but for 925-hPa moisture convergence (day^{-1}; shading) and Q700 (K day^{-1}; contours).

between 5°S and 5°N and normalized by their corresponding maxima. To quantify zonal structural asymmetries, we will first propose objective indices and then investigate how the simulated indices are related to simulated MJO propagation skills in all 24 GCM simulations.

a. Relative intensity of the low-level Rossby westerly versus Kelvin easterly waves

Figure 5a shows the composite equatorial U850 profiles simulated in the good and poor models along with the corresponding observations. To quantify the zonal asymmetry in the equatorial U850, we define the relative strength of the Rossby versus Kelvin wave components by the ratio of the maximum westerly speed $U_{\max}$ versus the minimum easterly speed $U_{\min}$. This ratio is called the Rossby–Kelvin (R-K) intensity index.

Figure 5b shows a robust correlation between the R-K intensity index and the MJO eastward propagation skill (CC = 0.76). The R-K intensity ratio simulated in the models ranges from −0.6 to −2.4, while the observed

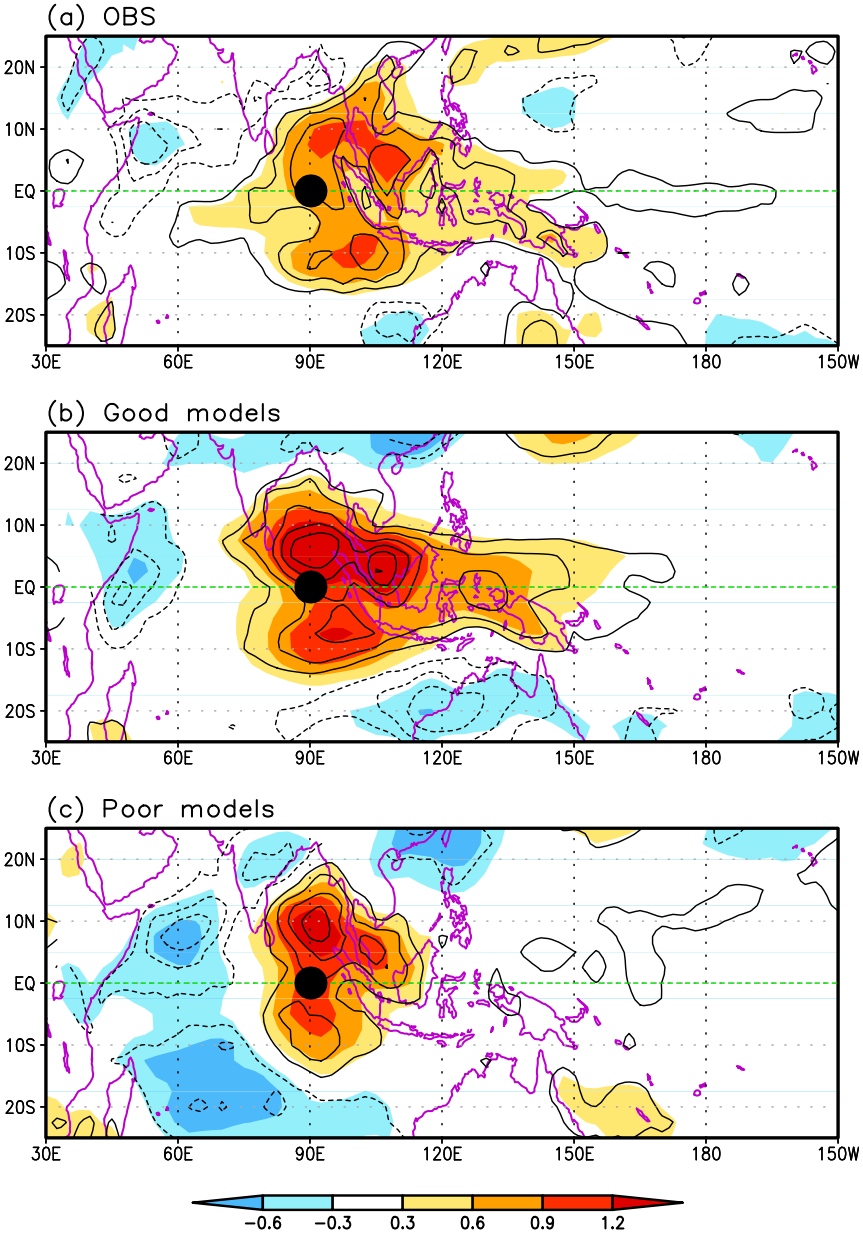

FIG. 4. As in Fig. 2, but for the $EPT_{1000–700}$ (K; shading) and specific humidity at 850 hPa (g kg^{-1}; contours).

value is −0.8. The results in Fig. 5b indicate that the models that simulated a more realistic R-K intensity ratio (or the relative strength of the Rossby versus Kelvin wave components) reproduce better eastward propagation of MJO. The poor models have an excessively strong Rossby wave component.

The relative intensity of the Kelvin easterly versus Rossby westerly is not solely determined by the MJO heating over the IO. In many eastward propagation cases, there is a suppressed convection concurring in the equatorial WP, which can also enhance the Kelvin easterly by exciting descending dry Rossby waves (Matsuno 1966; Kim et al. 2014a).

b. *Zonal asymmetry in the lower-tropospheric diabatic heating*

Figure 6a exhibits the composite equatorial Q700 (i.e., Q700 averaged over 5°S–5°N) in observation and in good and poor models. The Q700 maximum is located to the east of the maximum precipitation (90°E) in the

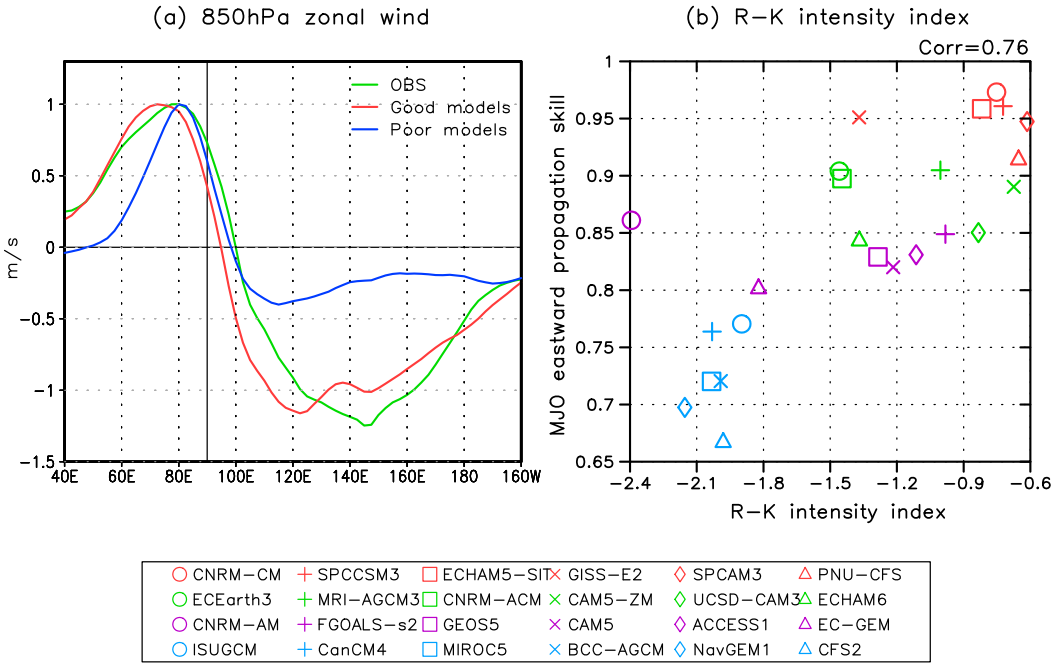

FIG. 5. (a) Longitudinal structure of the U850 in observation, composite of good models, and composite of poor models and (b) the relationship between MJO eastward propagation skill and R-K intensity index. The structure in (a) is regressed 20–70-day bandpass-filtered fields with reference to the precipitation anomaly in the EIO (10°S–10°N, 80°–100°E). The strengths are scaled to a fixed 3 mm day^{-1} precipitation rate. The regressed fields are averaged over 5°S–5°N and normalized by their maximum values. The MJO skill in (b) is measured by the averaged PCC skills of three regions shown in Figs. 1a–c. See text for more details in defining the R-K intensity index.

observation and good models, whereas it is located to the west of the precipitation center in poor models. Furthermore, the Q700 to the east of precipitation center (90°–140°E) is much stronger than that to the west (70°–90°E) in both observation and good models; however, the opposite is true in the poor models. In view of the differences between good and poor models, we propose a Q700 zonal asymmetric index using equatorial Q700 (Fig. 6a), which is calculated by the difference between the integrated positive heating rate to the east of precipitation center (integrated from 90° to 140°E) and that to the west (integrated from 70° to 90°E). The reason for choice of a larger extent to the east is because the Kelvin wave component has a larger zonal extent than the Rossby wave component.

The relationship between the simulated Q700 asymmetric index and MJO eastward propagation skill is shown in Fig. 6b. The statistically significant CC of 0.72 is obtained from 24 model simulations. The results suggest that eastward extension of heating from the major MJO precipitation center may be an indicator of the eastward propagation of MJO. The BLMC and the precipitation heating released in the shallow and congestus clouds are essential for the gradual transition from shallow congestus clouds to deep convection (e.g., Johnson et al. 1999; Johnson et al. 2015). This transition may facilitate eastward propagation of MJO activity.

c. *Zonal asymmetric equivalent potential temperature in the lower troposphere*

Figure 7a compares the composite equatorial $EPT_{1000–700}$ simulated in the good and poor models along with the corresponding observations. In both the observation and good models, the maximum centers of $EPT_{1000–700}$ are located about 15° of longitude to the east of the precipitation center, whereas it coincides with the precipitation center in the poor models' composite. The largest differences in $EPT_{1000–700}$ between the good and poor models are seen in the longitudinal extent between 110° and 150°E. For this reason, we define a zonal asymmetry index for $EPT_{1000–700}$, which is the $EPT_{1000–700}$ anomaly averaged between 110° and 150°E. Since the low-level EPT largely reflects moisture content, this index represents the degree of premoistening condition in front (to the east) of the MJO deep convection.

Figure 7b presents a close relationship between $EPT_{1000–700}$ asymmetric index (or the premoistening)

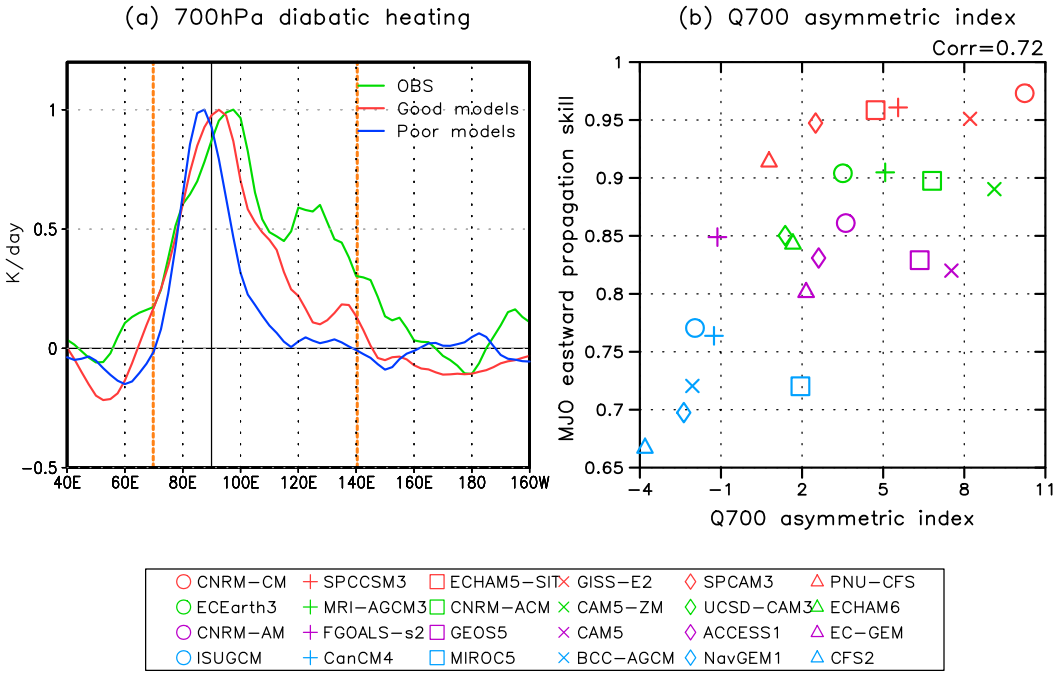

FIG. 6. As in Fig. 5, but for Q700. Orange vertical lines in (a) indicate the longitude range of Q700 asymmetric index. See text for more details in defining the Q700 asymmetric index.

and the MJO propagation fidelity in GCMs (CC = 0.70). The $EPT_{1000–700}$ index tends to be high in good models than in poor models, indicating that higher EPT occurring to the east of major precipitation center may favor MJO eastward propagation. The potential impact of this premoistening process on MJO propagation has been noted in the previous empirical studies (e.g., Kemball-Cook and Weare 2001).

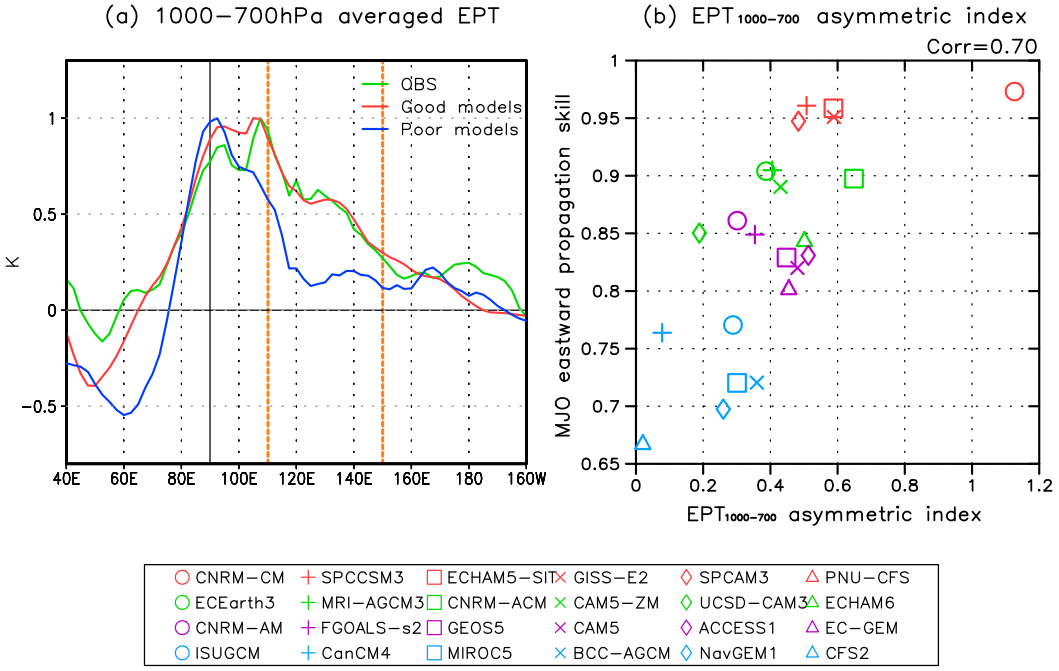

FIG. 7. As in Fig. 5, but for $EPT_{1000–700}$. Orange vertical lines in (a) indicate the longitude range of $EPT_{1000–700}$ asymmetric index. See text for more details in defining the $EPT_{1000–700}$ asymmetric index.

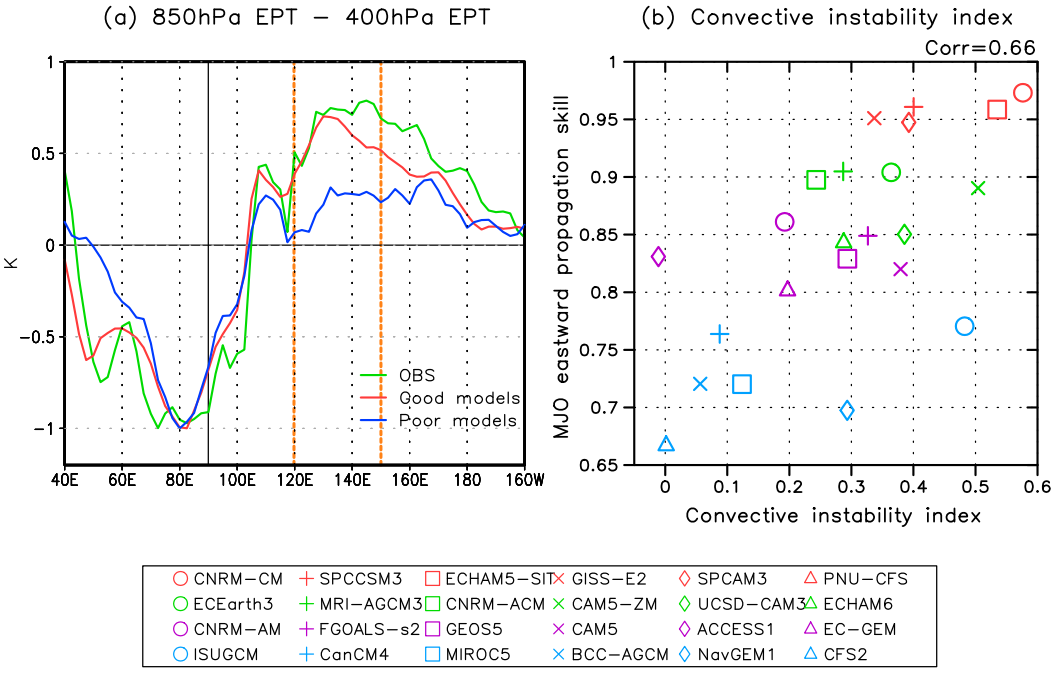

FIG. 8. As in Fig. 5, but for $EPT_{850} - EPT_{400}$ (convective instability index). The regressed fields are normalized by their minimum values. Orange vertical lines in (a) indicate the longitude range of convective instability index. See text for more details in defining the convective instability index.

d. Convective instability

Figure 8a compares the composite convective instability parameter [850-hPa EPT minus 400-hPa EPT ($EPT_{850} - EPT_{400}$)] simulated in the good and poor models. From 120° to 150°E, the observed high convective instability is simulated well by the good models, but not by the poor models. We define a convective instability index measuring the predestabilizing conditions in front of MJO deep convection, which is the mean convective instability parameter averaged between 120° and 150°E.

Figure 8b shows that the quality of simulated MJO eastward propagation is significantly linked to the simulated convective instability index with a positive CC of 0.66. This suggests that predestabilization of the MJO perturbation to the east of the MJO deep convection may pave the way for MJO eastward propagation. Using 40-yr ECMWF reanalysis data, Hsu and Li (2012) showed that the potential convective instability with sufficient lifting due to boundary layer convergence may help trigger shallow/congestus convection, favoring initiation of deep convection.

6. How the structural asymmetry leads to MJO eastward propagation

As shown in Fig. 9, when the MJO convection is centered at 90°E, the $EPT_{1000-700}$, and $EPT_{850} - EPT_{400}$ over the MC and equatorial WP in good models are much stronger than in the poor models. This is because the BLMC over the MC and equatorial WP is much stronger in the good models than in the poor models. The BLMC not only moistens the lower troposphere and creates convective instability through vertical mixing, but also generates vertical motion on the top of the boundary layer and induces heating in the lower troposphere (Q700) to the east of the MJO precipitation. This is evidenced by the large difference in Q700 to the east of the convective center from 90° to 140°E (Fig. 9c).

From an energetic point of view, the lower-tropospheric heating is vitally important for driving MJO eastward propagation for the following reasons. The generation of MJO available potential energy is determined by the covariance between diabatic heating Q' and temperature perturbation T' (Wang and Li 1994). Before calculation of the regression, we computed daily 3D fields of QT during the 20-yr period. Then a 20–70-day bandpass filter was applied ($Q'T'$). The lag zero regression pattern of $Q'T'$ is calculated against the 20–70-day bandpass-filtered rainfall averaged over the eastern equatorial IO (10°S–10°N, 80°–100°E). The regression amplitudes are scaled to a fixed 3 mm day^{-1} precipitation rate for comparison. As shown in Fig. 10b, the positive temperature anomalies tend to shift to the east of the major convection region. Therefore, the

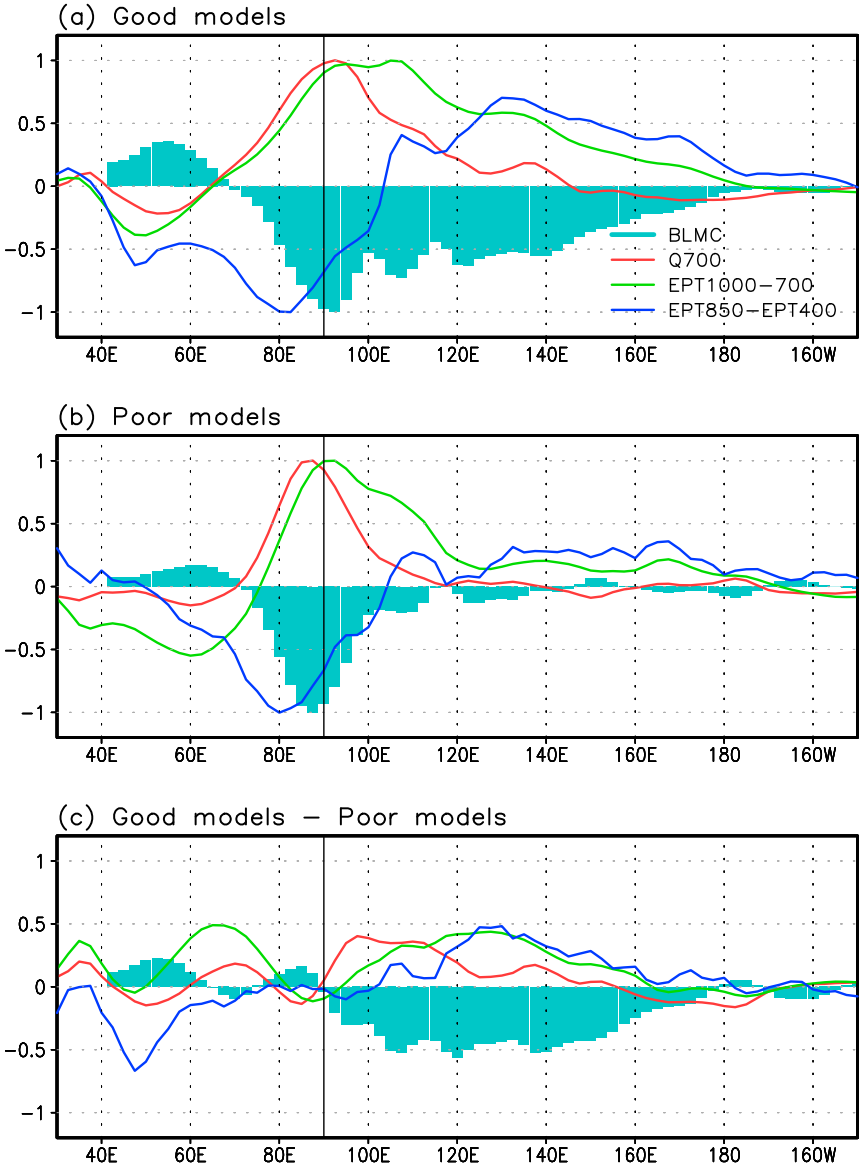

FIG. 9. Equatorial longitudinal structures of the 925-hPa moisture convergence (BLMC), Q700, $EPT_{1000–700}$, and $EPT_{850} - EPT_{400}$ for (a) composite of good models, (b) composite of poor models, and (c) difference between good and poor model composites. The structures are regressed 20–70-day bandpass-filtered fields with reference to the precipitation anomaly in the EIO (10°S–10°N, 80°–100°E). The strengths of all fields are scaled to a fixed 3 mm day^{-1} precipitation rate. All variables are averaged over 5°S–5°N and normalized by their maximum (minimum for $EPT_{850} - EPT_{400}$) values.

lower-tropospheric heating can generate MJO energy to the east of the MJO major convective center, leading to the MJO propagating eastward. The MJO energy generated in the major MJO convective regions, which is large for both the good and poor models, mainly contributes to the amplification of the MJO. As shown in Fig. 10c, the big difference in energy generation between the good and poor models is the zonal asymmetry: the generation in the poor models is nearly symmetric about the convection center, whereas in good models and observations the overall energy generation is stronger to the east than to the west of 90°E.

Our findings suggest the essential importance of the BLMC in the eastward propagation of the MJO. To elaborate this point further, we examine the evolution of the equatorial BLMC (averaged between 5°S and 5°N)

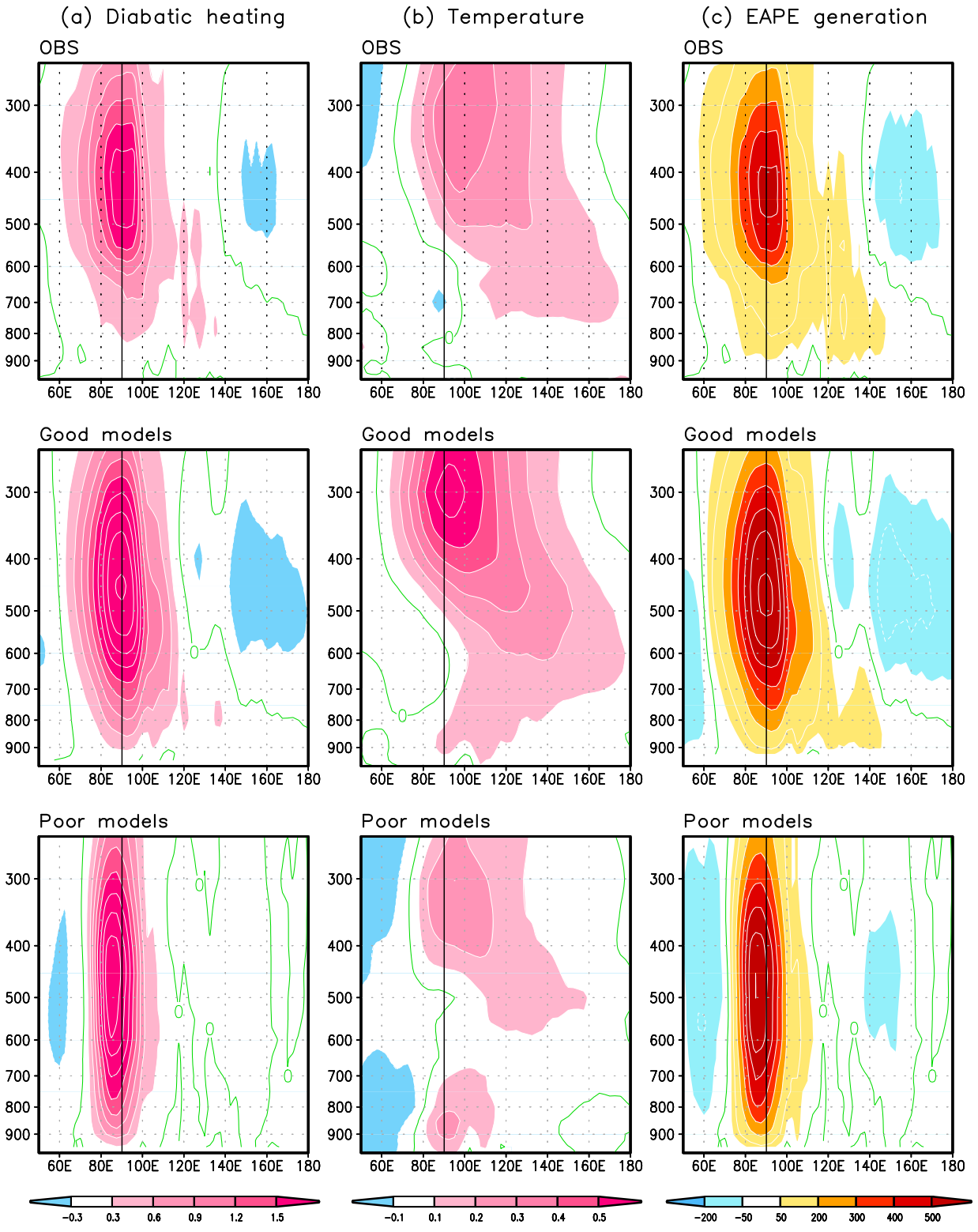

FIG. 10. Vertical structure of (a) diabatic heating (K day^{-1}), (b) temperature (K), and (c) eddy available potential energy (EAPE) generation ($Q'T'$) (K^2 day^{-1}) in observation, composite of good models, and composite of poor models. The structures are regressed 20–70-day bandpass-filtered fields with reference to the precipitation anomaly in the EIO (10°S–10°N, 80°–100°E). The regression strengths are scaled to a fixed 3 mm day^{-1} precipitation rate and averaged over 5°S–5°N.

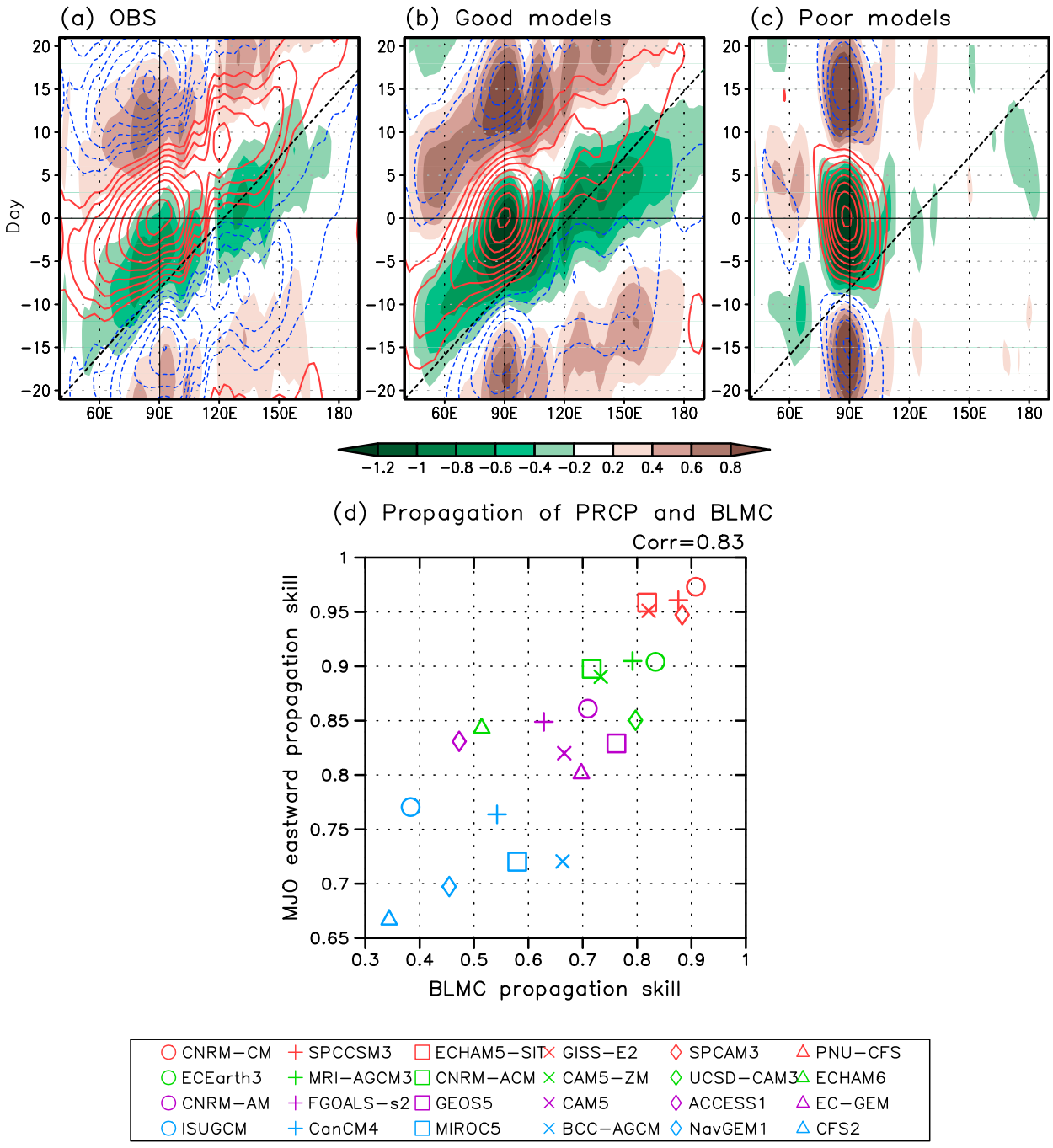

FIG. 11. Lead–lag correlation (contours; the contour interval is 0.1, solid red is positive, and dashed blue is negative) between 20–70-day bandpass-filtered precipitation and itself over the EIO (10°S–10°N, 80°–100°E) (i.e., as in Fig. 1a) and the lead–lag regression of 925-hPa moisture convergence (day^{-1}; shading) in (a) observation, (b) composite of good models, and (c) composite of poor models. (d) The relationship between simulated MJO eastward propagation skills and 925-hPa moisture convergence propagation skills. The regressed fields in (a)–(c) are averaged over 5°S–5°N and black dotted line represents 5 m s^{-1} eastward propagation speed. The 925-hPa moisture convergence propagation skill in (d) is measured by PCC between the observed and simulated propagation maps on the time–longitude domain (50°E–180°, from day −20 to day 20).

with reference to the MJO convection at the IO (90°E). It is noted that the BLMC propagates eastward continuously from 50°E to 180° with a speed of about 5 m s^{-1} in both observations (Fig. 11a) and good model simulations (Fig. 11b) whereas no propagation is found in the poor models (Fig. 11c). In general, the quality of the model-simulated eastward propagation of MJO precipitation is highly correlated with the simulated skill

of eastward propagation of BLMC (Fig. 11d). Notably, the propagation of the BLMC leads precipitation propagation by about 5 days (Fig. 11a). This phase leading is very well reproduced in the good models. The fact that the systematic eastward propagation of BLMC leads that of MJO deep convection suggests that the eastward propagation of the BLMC drives the eastward propagation of MJO through premoistening, predestabilization, and generating lower-tropospheric heating and MJO available potential energy to the east of the MJO main convection.

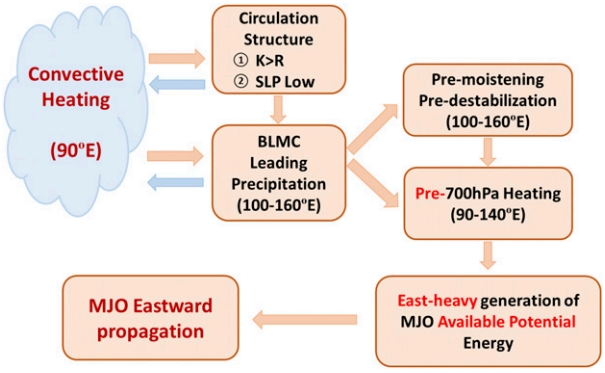

FIG. 12. Schematic diagram illustrating the mechanism for MJO eastward propagation.

7. Conclusions and discussion

a. Conclusions

Analysis of the diverse performances in the 24 GCM simulations of MJO reveals that the simulated MJO propagation is intrinsically associated with the simulated equatorial (averaged between 5°S and 5°N) east–west structural asymmetry with respect to the MJO convective center in the lower-tropospheric dynamic and thermodynamic structures, including 1) U850 (Fig. 2), 2) the BLMC and associated Q700 (Fig. 3), and 3) $EPT_{1000–700}$ and specific humidity at 850 hPa (Fig. 4). Based on the differences between the good and poor eastward-propagating models, four zonal structural asymmetry indices are proposed: 1) the lower-tropospheric zonal wind asymmetry measured by R-K intensity ratio (the ratio of maximum intensities of the equatorial westerly to easterly at 850 hPa); 2) the lower-tropospheric heating asymmetry defined by the Q700 (90°–140°E) minus Q700 (70°–90°E); 3) the premoistening index defined by the equatorial $EPT_{1000–700}$ averaged to the east of the convective center (90°E) between 110° and 150°E; and 4) the predestabilization index measured by the $EPT_{850} - EPT_{400}$ averaged between 120° and 150°E. All four diagnostics are significantly related to the models' MJO propagation skills (Figs. 5–8). The models having good eastward propagation of the BLMC are a robust indication of the realistic simulation of eastward propagation of the MJO convection (Fig. 11). More importantly, the propagation of the BLMC leads that of precipitation by about 5 days, suggesting a critical role of BLMC in MJO eastward propagation. The aforementioned lower-tropospheric structural asymmetries were observed and argued to be important for MJO eastward propagation. The present study finds, in GCM simulations, that the models that simulate these asymmetries well also have realistic eastward propagation of MJO whereas the models that failed to simulate these structural asymmetries do not simulate eastward propagation.

The schematic diagram shown in Fig. 12 summarizes how the zonal structural asymmetry shaped MJO eastward propagation. As demonstrated by theoretical model work of Wang et al. (2016), the coupled MJO convection and circulation system and the zonal structural asymmetries are essentially generated by a three-way interaction among collective convective heating, moisture, and large-scale wave and BL dynamics. The degree of the east–west asymmetry in the low-level circulation determines the zonal asymmetry in the BLMC. To the east of the MJO precipitation, the BLMC moistens the lower troposphere, creates convective instability, and induces lower-tropospheric heating (Q700). The zonal asymmetric dynamic and thermal structures and lower-tropospheric condensation heating result in a zonally asymmetric, east-heavy MJO available potential energy generation, thereby driving the MJO eastward. The results from the multimodel GCM simulations are consistent with the hypothesis that the BLMC and associated zonal structural asymmetries in the lower troposphere play a critical role in driving MJO eastward propagation.

b. Discussion

Concerning the relationship between the structural asymmetry and eastward propagation, an alternative hypothesis is that the presence of a propagating convection heating may cause the zonal asymmetry in the lower-tropospheric dynamic and thermodynamic fields. A given heat source can produce a Gill-like pattern with a Kelvin wave component to its east and a Rossby wave component to its west (Gill 1980). Presumably, if a Gill-type convection and circulation system is moved eastward, the corresponding structure may be changed. When a fixed heat source is forced to move eastward, it is equivalent to add a mean westward flow in the Gill model. Because of the mean flow effects, the low-level Kelvin wave propagation speed would decrease while Rossby wave speed would increase. For a given damping rate, this would shorten the extent of the Kelvin wave

component while increasing the zonal extent of the Rossby wave component. However, it is not clear how this would affect the zonal wind speed (the R-K intensity ratio) because the equatorial zonal wind speed is determined by the meridional pressure gradients and a zonal mean flow may not change them.

On the other hand, the MJO structure is generated by interactive convective heating. The interaction of dynamics, moisture, and convective heating provides a key to understanding the circulation asymmetry. Using a general theoretical model for the MJO, Wang and Chen (2017) have shown that different cumulus parameterization schemes (e.g., simplified Kuo and Betts–Miller) or different parameters in the Betts–Miller scheme (e.g., the convective adjustment time scale) can produce different MJO structural asymmetries, especially different R-K intensity ratios. They have also demonstrated that the MJO propagation speed is proportional to the R-K intensity ratio.

The present diagnostic work, using multimodel results, reveals 1) that models with different parameterization schemes and parameter values can produce variety of structural asymmetry, and 2) that better simulated structural asymmetry corresponds to better eastward propagation. A variety of structural asymmetries seen from the 24 models studied here may arise from different representations of the convective heating, thereby resulting in different propagation characteristics. These GCM model results seem to be consistent with the aforementioned theoretical model results.

The MSE tendency has been conveniently used to explain the eastward propagation of MJO convection because the vertically integrated MSE coincides with the MJO convection. The MSE budget results suggest that the MJO eastward propagation is caused by horizontal and vertical advection of the MJO MSE (e.g., Maloney 2009; DeMott et al. 2014). The MSE diagnostics provide a kinematic explanation for eastward propagation but may not reveal the root cause of the eastward propagation.

Explanation of the root cause of the MJO eastward propagation requires addressing, in the first place, why the MJO has a mixed Kelvin–Rossby wave structure and how the westward-propagating Rossby waves and eastward-propagating Kelvin waves can be coupled together with convection and select preferred eastward propagation. Recently, Wang and Chen (2017) and Liu and Wang (2017) implemented the moisture feedback mechanism into the frictionally coupled Kelvin–Rossby wave theory, which leads to a general three-way interaction theory (Wang et al. 2016). The three-way interaction refers to the interaction among convection, moisture, and dynamics (the equatorial wave and boundary layer dynamics), which is the core dynamics of the MJO. In this general framework, six existing simplified versions of cumulus parameterization schemes are accommodated. It was shown that, no matter which convective parameterization scheme is used, without the boundary layer effect, a given initial Gill-like disturbance will be decoupled: the Kelvin wave moves eastward and the Rossby wave moves westward. It is the presence of the boundary layer frictional convergence associated with the Kelvin and Rossby waves that produces a joint BLMC field, which can couple the waves and convection together, and select eastward propagation for the K-R wave packet. The moisture feedback under a Betts–Miller scheme is shown to reinforce the coupling between the precipitation heating and Rossby waves, and thus the Rossby wave component is enhanced in the MJO, thereby slowing down the eastward propagation and resulting in more realistic horizontal structure and oscillation periodicity.

In addition to the three-way interaction theory and the moisture mode theory, various other processes have been identified or speculated to play significant roles in MJO propagation, including the air–sea interaction (Flatau et al. 1997; Wang and Xie 1998; Waliser et al. 1999; Kemball-Cook and Wang 2001; Wang and Zhang 2002; Fu and Wang 2004; Sperber et al. 2005; DeMott et al. 2014; Klingaman and Woolnough 2014), the stratiform cloud–wave interaction (Mapes 2000; Khouider and Majda 2006; Kuang 2008; Fu and Wang 2009; Seo and Wang 2010), and moisture or moist static energy transport (Maloney 2009; Maloney et al. 2010; Andersen and Kuang 2012; Hsu and Li 2012; Kim et al. 2014a; Pritchard and Bretherton 2014). How these processes affect the MJO structure remain to be studied.

Our findings suggest the essential importance of the zonally asymmetric low-level circulation and the BLMC in the eastward propagation of MJO. Since the lower-tropospheric structural asymmetry in circulation and diabatic heating are intimately linked to MJO eastward propagation, the performance in the simulation of the lower-tropospheric asymmetry in dynamical and thermodynamic structures calls for attention. Better representation of the interactions between the BLMC and cumulus congestus cloud precipitation, the convective mixing, low-cloud feedback and BL parameterization may be critical for better simulation of the MJO. Our results also suggest that to help identify models' deficiencies, it may be advantageous to implement some dynamics-oriented diagnostics presented in this paper into the metrics for evaluation of MJO simulation (Waliser et al. 2009).

Acknowledgments. This work is supported by the support from the National Science Foundation (Division of Atmospheric and Geospace Sciences Award AGS-1540783) and the NOAA/DYNAMO Award NA13OAR4310167 and NOAA/CVP Award NA15OAR4310177, as well as the Global Research Laboratory (GRL) Program of the Korean Ministry of Education, Science and Technology (MEST; 2011-0021927).

REFERENCES

Adames, Á. F., and J. M. Wallace, 2014: Three-dimensional structure and evolution of the MJO and its relation to the mean flow. *J. Atmos. Sci.*, **71**, 2007–2026, doi:10.1175/JAS-D-13-0254.1.

——, and D. Kim, 2016: The MJO as a dispersive, convectively coupled moisture wave: Theory and observations. *J. Atmos. Sci.*, **73**, 913–941, doi:10.1175/JAS-D-15-0170.1.

Andersen, J. A., and Z. Kuang, 2012: Moist static energy budget of MJO-like disturbances in the atmosphere of a zonally symmetric aquaplanet. *J. Climate*, **25**, 2782–2804, doi:10.1175/JCLI-D-11-00168.1.

Bao, Q., and Coauthors, 2013: The Flexible Global Ocean–Atmosphere–Land System Model, spectral version 2: FGOALS-s2. *Adv. Atmos. Sci.*, **30**, 561–576, doi:10.1007/s00376-012-2113-9.

Benedict, J. J., E. D. Maloney, A. H. Sobel, and D. M. W. Frierson, 2014: Gross moist stability and MJO simulation skill in three full-physics GCMs. *J. Atmos. Sci.*, **71**, 3327–3349, doi:10.1175/JAS-D-13-0240.1.

Bretherton, C. S., M. E. Peters, and L. E. Back, 2004: Relationships between water vapor path and precipitation over the tropical oceans. *J. Climate*, **17**, 1517–1528, doi:10.1175/1520-0442(2004)017<1517:RBWVPA>2.0.CO;2.

Côté, J., S. Gravel, A. Méthot, A. Patoine, M. Roch, and A. Staniforth, 1998: The operational CMC-MRB Global Environmental Multiscale (GEM) model. Part I: Design considerations and formulation. *Mon. Wea. Rev.*, **126**, 1373–1395, doi:10.1175/1520-0493(1998)126<1373:TOCMGE>2.0.CO;2.

Dee, D. P., and Coauthors, 2011: The ERA-Interim reanalysis: Configuration and performance of the data assimilation system. *Quart. J. Roy. Meteor. Soc.*, **137**, 553–597, doi:10.1002/qj.828.

Del Genio, A. D., Y. Chen, D. Kim, and M.-S. Yao, 2012: The MJO transition from shallow to deep convection in *CloudSat/CALIPSO* data and GISS GCM simulations. *J. Climate*, **25**, 3755–3770, doi:10.1175/JCLI-D-11-00384.1.

DeMott, C. A., C. Stan, D. A. Randall, and M. D. Branson, 2014: Intraseasonal variability in coupled GCMs: The roles of ocean feedbacks and model physics. *J. Climate*, **27**, 4970–4995, doi:10.1175/JCLI-D-13-00760.1.

Flatau, M., P. J. Flatau, P. Phoebus, and P. P. Niiler, 1997: The feedback between equatorial convection and local radiative and evaporative processes: The implications for intraseasonal oscillations. *J. Atmos. Sci.*, **54**, 2373–2386, doi:10.1175/1520-0469(1997)054<2373:TFBECA>2.0.CO;2.

Fu, X., and B. Wang, 2004: Differences of boreal summer intraseasonal oscillations simulated in an atmosphere–ocean coupled model and an atmosphere-only model. *J. Climate*, **17**, 1263–1271, doi:10.1175/1520-0442(2004)017<1263:DOBSIO>2.0.CO;2.

——, and ——, 2009: Critical roles of the stratiform rainfall in sustaining the Madden–Julian oscillation: GCM experiments. *J. Climate*, **22**, 3939–3959, doi:10.1175/2009JCLI2610.1.

Gill, A. E., 1980: Some simple solutions for heat-induced tropical circulation. *Quart. J. Roy. Meteor. Soc.*, **106**, 447–462, doi:10.1002/qj.49710644905.

Hannah, W. M., and E. D. Maloney, 2011: The role of moisture–convection feedbacks in simulating the Madden–Julian oscillation. *J. Climate*, **24**, 2754–2770, doi:10.1175/2011JCLI3803.1.

Hendon, H. H., and M. L. Salby, 1994: The life cycle of the Madden–Julian oscillation. *J. Atmos. Sci.*, **51**, 2225–2237, doi:10.1175/1520-0469(1994)051<2225:TLCOTM>2.0.CO;2.

Hsu, P.-C., and T. Li, 2012: Role of the boundary layer moisture asymmetry in causing the eastward propagation of the Madden–Julian oscillation. *J. Climate*, **25**, 4914–4931, doi:10.1175/JCLI-D-11-00310.1.

Huffman, G. J., and D. T. Bolvin, 2013: Version 1.2 GPCP one-degree daily precipitation data set documentation. 27 pp. [Available online at ftp://meso.gsfc.nasa.gov/pub/1dd-v1.2/1DD_v1.2_doc.pdf.]

Jiang, X., and Coauthors, 2015: Vertical structure and physical processes of the Madden–Julian oscillation: Exploring key model physics in climate simulations. *J. Geophys. Res.*, **120**, 4718–4748, doi:10.1002/2014JD022375.

Johnson, R. H., T. M. Rickenbach, S. A. Rutledge, P. E. Ciesielski, and W. H. Schubert, 1999: Trimodal characteristics of tropical convection. *J. Climate*, **12**, 2397–2418, doi:10.1175/1520-0442(1999)012<2397:TCOTC>2.0.CO;2.

——, J. H. Ruppert Jr., and M. Katsumata, 2015: Sounding-based thermodynamic budgets for DYNAMO. *J. Atmos. Sci.*, **72**, 598–622, doi:10.1175/JAS-D-14-0202.1.

Jones, C., and B. C. Weare, 1996: The role of low-level moisture convergence and ocean latent heat flux in the Madden–Julian oscillation: An observational analysis using ISCCP data and ECMWF analyses. *J. Climate*, **9**, 3086–3104, doi:10.1175/1520-0442(1996)009<3086:TROLLM>2.0.CO;2.

Katsumata, M., R. H. Johnson, and P. E. Ciesielski, 2009: Observed synoptic-scale variability during the developing phase of an ISO over the Indian Ocean during MISMO. *J. Atmos. Sci.*, **66**, 3434–3448, doi:10.1175/2009JAS3003.1.

Kemball-Cook, S., and B. Wang, 2001: Equatorial waves and air–sea interaction in the boreal summer intraseasonal oscillation. *J. Climate*, **14**, 2923–2942, doi:10.1175/1520-0442(2001)014<2923:EWAASI>2.0.CO;2.

——, and B. C. Weare, 2001: The onset of convection in the Madden–Julian oscillation. *J. Climate*, **14**, 780–793, doi:10.1175/1520-0442(2001)014<0780:TOOCIT>2.0.CO;2.

Khairoutdinov, M., C. DeMott, and D. Randall, 2008: Evaluation of the simulated interannual and subseasonal variability in an AMIP-style simulation using the CSU multiscale modeling framework. *J. Climate*, **21**, 413–431, doi:10.1175/2007JCLI1630.1.

Khouider, B., and A. J. Majda, 2006: A simple multicloud parameterization for convectively coupled tropical waves. Part I: Linear analysis. *J. Atmos. Sci.*, **63**, 1308–1323, doi:10.1175/JAS3677.1.

Kikuchi, K., and Y. N. Takayabu, 2004: The development of organized convection associated with the MJO during TOGA COARE IOP: Trimodal characteristics. *Geophys. Res. Lett.*, **31**, L10101, doi:10.1029/2004GL019601.

——, B. Wang, and Y. Kajikawa, 2012: Bimodal representation of the tropical intraseasonal oscillation. *Climate Dyn.*, **38**, 1989–2000, doi:10.1007/s00382-011-1159-1.

Kim, D., and Coauthors, 2009: Application of MJO simulation diagnostics to climate models. *J. Climate*, **22**, 6413–6436, doi:10.1175/2009JCLI3063.1.

——, A. H. Sobel, A. D. Del Genio, Y. Chen, S. J. Camargo, M.-S. Yao, M. Kelley, and L. Nazarenko, 2012: The tropical subseasonal variability simulated in the NASA GISS general circulation model. *J. Climate*, **25**, 4641–4659, doi:10.1175/JCLI-D-11-00447.1.

——, J.-S. Kug, and A. H. Sobel, 2014a: Propagating versus nonpropagating Madden–Julian oscillation events. *J. Climate*, **27**, 111–125, doi:10.1175/JCLI-D-13-00084.1.

——, and Coauthors, 2014b: Process-oriented MJO simulation diagnostic: Moisture sensitivity of simulated convection. *J. Climate*, **27**, 5379–5395, doi:10.1175/JCLI-D-13-00497.1.

Klingaman, N. P., and S. J. Woolnough, 2014: The role of air–sea coupling in the simulation of the Madden–Julian oscillation in the Hadley Centre model. *Quart. J. Roy. Meteor. Soc.*, **140**, 2272–2286, doi:10.1002/qj.2295.

——, X. Jiang, P. K. Xavier, J. Petch, D. Waliser, and S. J. Woolnough, 2015a: Vertical structure and physical processes of the Madden–Julian oscillation: Synthesis and summary. *J. Geophys. Res. Atmos.*, **120**, 4671–4689, doi:10.1002/2015JD023196.

——, and Coauthors, 2015b: Vertical structure and physical processes of the Madden-Julian oscillation: Linking hindcast fidelity to simulated diabatic heating and moistening. *J. Geophys. Res. Atmos.*, **120**, 4690–4717, doi:10.1002/2014JD022374.

Kuang, Z., 2008: A moisture-stratiform instability for convectively coupled waves. *J. Atmos. Sci.*, **65**, 834–854, doi:10.1175/2007JAS2444.1.

Lin, J., B. E. Mapes, M. Zhang, and M. Newman, 2004: Stratiform precipitation, vertical heating profiles, and the Madden–Julian Oscillation. *J. Atmos. Sci.*, **61**, 296–309, doi:10.1175/1520-0469(2004)061<0296:SPVHPA>2.0.CO;2.

Liu, F., and B. Wang, 2017: Effects of moisture feedback in a frictional coupled Kelvin– Rossby wave model and implication in the Madden–Julian oscillation dynamics. *Climate Dyn.*, **48**, 513–522, doi:10.1007/s00382-016-3090-y.

Madden, R. A., and P. R. Julian, 1972: Description of global-scale circulation cells in the tropics with a 40–50 day period. *J. Atmos. Sci.*, **29**, 1109–1123, doi:10.1175/1520-0469(1972)029<1109:DOGSCC>2.0.CO;2.

Maloney, E. D., 2009: The moist static energy budget of a composite tropical intraseasonal oscillation in a climate model. *J. Climate*, **22**, 711–729, doi:10.1175/2008JCLI2542.1.

——, A. H. Sobel, and W. M. Hannah, 2010: Intraseasonal variability in an aquaplanet general circulation model. *J. Adv. Model. Earth Syst.*, **2** (5), doi:10.3894/JAMES.2010.2.5.

Mapes, B. E., 2000: Convective inhibition, subgrid-scale triggering energy, and stratiform instability in a toy tropical wave model. *J. Atmos. Sci.*, **57**, 1515–1535, doi:10.1175/1520-0469(2000)057<1515:CISSTE>2.0.CO;2.

Matsuno, T., 1966: Quasi-geostrophic motions in the equatorial area. *J. Meteor. Soc. Japan*, **44**, 25–43, doi:10.2151/jmsj1965.44.1_25.

Matthews, A. J., 2000: Propagation mechanisms for the Madden–Julian oscillation. *Quart. J. Roy. Meteor. Soc.*, **126**, 2637–2651, doi:10.1002/qj.49712656902.

Merryfield, W. J., and Coauthors, 2013: The Canadian seasonal to interannual prediction system. Part I: Models and initialization. *Mon. Wea. Rev.*, **141**, 2910–2945, doi:10.1175/MWR-D-12-00216.1.

Molod, A., L. Takacs, L. M. Suarez, J. Bacmeister, I.-S. Song, and A. Eichmann, 2012: The GEOS-5 atmospheric general circulation model: Mean climate and development from MERRA to Fortuna. NASA Technical Report Series on Global Modeling and Data Assimilation, NASA-TM-2012-104606, Vol. 28, 117 pp.

Neale, R. B., and Coauthors, 2012: Description of the NCAR Community Atmosphere Model: CAM 5.0. Tech. Rep. NCAR/TN-486+STR, 274 pp. [Available online at www.cesm.ucar.edu/models/cesm1.0/cam/docs/description/cam5_desc.pdf.]

Petch, J., D. Waliser, X. Jiang, P. K. Xavier, and S. Woolnough, 2011: A global model intercomparison of the physical processes associated with the Madden-Julian Oscillation. *GEWEX News*, No. 8, International GEWEX Project Office, Silver Spring, MD, 3–5.

Pritchard, M. S., and C. S. Bretherton, 2014: Causal evidence that rotational moisture advection is critical to the superparameterized Madden–Julian oscillation. *J. Atmos. Sci.*, **71**, 800–815, doi:10.1175/JAS-D-13-0119.1.

Raymond, D. J., and Ž. Fuchs, 2009: Moisture modes and the Madden–Julian oscillation. *J. Climate*, **22**, 3031–3046, doi:10.1175/2008JCLI2739.1.

——, S. Sessions, A. Sobel, and Z. Fuchs, 2009: The mechanics of gross moist stability. *J. Adv. Model. Earth Syst.*, **1** (9), doi:10.3894/JAMES.2009.1.9.

Rui, H., and B. Wang, 1990: Development characteristics and dynamic structure of tropical intraseasonal convection anomalies. *J. Atmos. Sci.*, **47**, 357–379, doi:10.1175/1520-0469(1990)047<0357:DCADSO>2.0.CO;2.

Saha, S., and Coauthors, 2006: The NCEP Climate Forecast System. *J. Climate*, **19**, 3483–3517, doi:10.1175/JCLI3812.1.

——, and Coauthors, 2014: The NCEP Climate Forecast System version 2. *J. Climate*, **27**, 2185–2208, doi:10.1175/JCLI-D-12-00823.1.

Salby, M. L., H. H. Hendon, and R. R. Garcia, 1994: Planetary-scale circulations in the presence of climatological and wave-induced heating. *J. Atmos. Sci.*, **51**, 2344–2367, doi:10.1175/1520-0469(1994)051<2344:PSCITP>2.0.CO;2.

Schmidt, G. A., and Coauthors, 2014: Configuration and assessment of the GISS ModelE2 contributions to the CMIP5 archive. *J. Adv. Model. Earth Syst.*, **6**, 141–184, doi:10.1002/2013MS000265.

Seo, K.-H., and W. Wang, 2010: The Madden–Julian oscillation simulated in the NCEP Climate Forecast System model: The importance of stratiform heating. *J. Climate*, **23**, 4770–4793, doi:10.1175/2010JCLI2983.1.

Sobel, A. H., and E. D. Maloney, 2012: An idealized semi-empirical framework for modeling the Madden–Julian oscillation. *J. Atmos. Sci.*, **69**, 1691–1705, doi:10.1175/JAS-D-11-0118.1.

——, and ——, 2013: Moisture modes and the eastward propagation of the MJO. *J. Atmos. Sci.*, **70**, 187–192, doi:10.1175/JAS-D-12-0189.1.

Song, X., and G. J. Zhang, 2011: Microphysics parameterization for convective clouds in a global climate model: Description and single-column model tests. *J. Geophys. Res.*, **116**, D02201, doi:10.1029/2010JD014833.

Sperber, K. R., 2003: Propagation and the vertical structure of the Madden–Julian oscillation. *Mon. Wea. Rev.*, **131**, 3018–3037, doi:10.1175/1520-0493(2003)131<3018:PATVSO>2.0.CO;2.

——, S. Gualdi, S. Legutke, and V. Gayler, 2005: The Madden–Julian oscillation in ECHAM4 coupled and uncoupled general circulation models. *Climate Dyn.*, **25**, 117–140, doi:10.1007/s00382-005-0026-3.

Stan, C., M. Khairoutdinov, C. A. DeMott, V. Krishnamurthy, D. M. Straus, D. A. Randall, J. L. Kinter, and J. Shukla, 2010: An ocean–atmosphere climate simulation with an embedded cloud resolving model. *Geophys. Res. Lett.*, **37**, L01702, doi:10.1029/2009GL040822.

Stevens, B., and Coauthors, 2013: Atmospheric component of the MPI-M Earth System Model: ECHAM6. *J. Adv. Model. Earth Syst.*, **5**, 146–172, doi:10.1002/jame.20015.

Thayer-Calder, K., and D. A. Randall, 2009: The role of convective moistening in the Madden–Julian oscillation. *J. Atmos. Sci.*, **66**, 3297–3312, doi:10.1175/2009JAS3081.1.

Tian, B., D. E. Waliser, E. Fetzer, B. Lambrigtsen, Y. Yung, and B. Wang, 2006: Vertical moist thermodynamic structure and spatial–temporal evolution of the Madden–Julian oscillation in AIRS observations. *J. Atmos. Sci.*, **63**, 2462–2485, doi:10.1175/JAS3782.1.

Tseng, W.-L., B.-J. Tsuang, N. Keenlyside, H.-H. Hsu, and C.-Y. Tu, 2015: Resolving the upper-ocean warm layer improves the simulation of the Madden–Julian oscillation. *Climate Dyn.*, **44**, 1487–1503, doi:10.1007/s00382-014-2315-1.

Virts, K. S., and J. M. Wallace, 2010: Annual, interannual, and intraseasonal variability of tropical tropopause transition layer cirrus. *J. Atmos. Sci.*, **67**, 3097–3112, doi:10.1175/2010JAS3413.1.

Voldoire, A., and Coauthors, 2013: The CNRM-CM5.1 global climate model: Description and basic evaluation. *Climate Dyn.*, **40**, 2091–2121, doi:10.1007/s00382-011-1259-y.

Waliser, D. E., 2006: Intraseasonal variations. *The Asian Monsoon*, B. Wang, Ed., Springer, 203–257.

——, K. M. Lau, and J. H. Kim, 1999: The influence of coupled sea surface temperatures on the Madden–Julian oscillation: A model perturbation experiment. *J. Atmos. Sci.*, **56**, 333–358, doi:10.1175/1520-0469(1999)056<0333:TIOCSS>2.0.CO;2.

——, and Coauthors, 2009: MJO simulation diagnostics. *J. Climate*, **22**, 3006–3030, doi:10.1175/2008JCLI2731.1.

Wang, B., 1988: Dynamics of tropical low-frequency waves: An analysis of the moist Kelvin wave. *J. Atmos. Sci.*, **45**, 2051–2065, doi:10.1175/1520-0469(1988)045<2051:DOTLFW>2.0.CO;2.

——, and H. Rui, 1990: Dynamics of the coupled moist Kelvin–Rossby wave on an equatorial β-plane. *J. Atmos. Sci.*, **47**, 397–413, doi:10.1175/1520-0469(1990)047<0397:DOTCMK>2.0.CO;2.

——, and T. Li, 1994: Convective interaction with boundary-layer dynamics in the development of a tropical intraseasonal system. *J. Atmos. Sci.*, **51**, 1386–1400, doi:10.1175/1520-0469(1994)051<1386:CIWBLD>2.0.CO;2.

——, and X. Xie, 1998: Coupled modes of the warm pool climate system. Part I: The role of air–sea interaction in maintaining Madden–Julian oscillation. *J. Climate*, **11**, 2116–2135, doi:10.1175/1520-0442-11.8.2116.

——, and Q. Zhang, 2002: Pacific–East Asian teleconnection. Part II: How the Philippine Sea anomalous anticyclone is established during El Niño development. *J. Climate*, **15**, 3252–3265, doi:10.1175/1520-0442(2002)015<3252:PEATPI>2.0.CO;2.

——, and G. Chen, 2017: A general theoretical framework for understanding essential dynamics of Madden–Julian oscillation. *Climate Dyn.*, doi:10.1007/s00382-016-3448-1, in press.

——, F. Liu, and G. Chen, 2016: A trio-interaction theory for Madden-Julia Oscillation. *Geosci. Lett.*, **3** (34), doi:10.1186/s40562-016-0066-z.

Watanabe, M., and Coauthors, 2010: Improved climate simulation by MIROC5: Mean states, variability, and climate sensitivity. *J. Climate*, **23**, 6312–6335, doi:10.1175/2010JCLI3679.1.

Wu, T., and Coauthors, 2010: The Beijing Climate Center atmospheric general circulation model: Description and its performance for the present-day climate. *Climate Dyn.*, **34**, 123–147, doi:10.1007/s00382-008-0487-2.

Wu, X., and L. Deng, 2013: Comparison of moist static energy and budget between the GCM-simulated Madden–Julian oscillation and observations over the Indian Ocean and western Pacific. *J. Climate*, **26**, 4981–4993, doi:10.1175/JCLI-D-12-00607.1.

Xavier, P. K., 2012: Intraseasonal convective moistening in CMIP3 models. *J. Climate*, **25**, 2569–2577, doi:10.1175/JCLI-D-11-00427.1.

Yukimoto, S., and Coauthors, 2012: A new global climate model of the Meteorological Research Institute: MRI-CGCM3—Model description and basic performance. *J. Meteor. Soc. Japan*, **90A**, 23–64, doi:10.2151/jmsj.2012-A02.

Zhang, G. J., and M. Mu, 2005: Simulation of the Madden–Julian oscillation in the NCAR CCM3 using a revised Zhang–McFarlane convection parameterization scheme. *J. Climate*, **18**, 4046–4064, doi:10.1175/JCLI3508.1.

Zhu, H., H. Hendon, M. Dix, Z. Sun, G. Dietachmayer, and K. Puri, 2013: Vertical structure and diabatic processes of the MJO, A global model inter-comparison Project: Preliminary results from ACCESS model. *CAWCR Research Letters*, Vol. 10, Bureau of Meteorology, Melbourne, Australia, 34–38. [Available online at www.cawcr.gov.au/researchletters/CAWCR_Research_Letters_10.pdf.]